

Actuator Line Method for Ducted Fan Applications

M-A. Breault, G. Dumas *

LMFN CFD Laboratory, Department of Mechanical Engineering
Laval University, Quebec, Quebec, Canada

F. Marois, M. Béland, M. Lapalme, G. Biron
Bell Textron Canada Ltd., Mirabel, Quebec, Canada

Abstract: An Actuator Line Method (ALM) based on integral velocity sampling is developed for application to ducted fans. In this work, the lifting surface is replaced by momentum source terms in the unsteady Reynolds-averaged Navier-Stokes equations. The source terms are computed at discrete locations along the blade's span before being spread on the mesh using a nonisotropic Gaussian kernel allowing the source terms distribution to mimic the geometrical attributes of the blade at that location. The determination of the local effective freestream vector, a common difficulty of ALM approaches, is done with an integral velocity sampling that accounts for the blade's local induced velocity. Including the projection function in the computation of the effective freestream velocity vector makes the formulation more general and removes the ambiguity surrounding the determination of the local velocity. The method is first validated against experimental data from Caradonna & Tung [1] for the open rotor case, and the influence of the nonisotropic Gaussian kernel parameters on the solution is then presented. The appropriateness of the method when applied to ducted geometries is validated against experimental data from wind tunnel testing of a ducted fan and against blade-resolved CFD. The results obtained for the ducted geometry show that the ALM is able to account for the presence of the duct, but that the effective expansion ratio of the duct in the ALM simulations is smaller than its blade-resolved equivalent.

Keywords: Actuator Line Method, Computational Fluid Dynamics, Rotor Replacement Techniques, Ducted fans

*Professor, corresponding author: Guy.Dumas@gmc.ulaval.ca

Nomenclature

a	=	Projection factor
c	=	Blade chord, m
C_D	=	Drag coefficient
C_L	=	Lift coefficient
C_P	=	Power coefficient, $P / \pi \rho \Omega^3 R^5$
c_p	=	Pressure coefficient, $2(p - p_\infty) / \rho U_\infty^2$
C_T	=	Thrust coefficient, $T / \pi \rho \Omega^2 R^4$
g	=	Volumetric force spreading kernel
J	=	Advance ratio, $U_\infty / \Omega R$
Ma	=	Mach number
N_B	=	Number of blades
R	=	Rotor radius, m
Re	=	Reynolds number
t	=	Blade thickness, m
T_{rotor}	=	Rotor thrust, N
T_{total}	=	Total thrust, N
\vec{U}_∞	=	Freestream velocity vector, m/s
U_c	=	Climb speed, m/s
V	=	Velocity sampling integration volume, m ³
V_{tip}	=	Blade tip speed, m/s
v_i	=	Induced velocity at the rotor plane, m/s
w	=	Velocity at the diffuser exit plane, m/s
α_{geo}	=	Geometric angle of attack, °
Δx_{ref}	=	Characteristic mesh size
δr	=	Panel width, m
ε	=	Gaussian width
Ω	=	Angular velocity, rad/s
Ψ	=	Azimuthal position, °
σ	=	Solidity, $N_B c / \pi R$
σ_d	=	Effective expansion ratio
Θ	=	Collective pitch, °

Superscript

' = Variable per unit length

Subscripts

0	=	Control point center
c	=	Coordinate along the panel chord
i	=	Control point index
j	=	Cell centroid index
r	=	Coordinate along the panel span
t	=	Coordinate along the panel thickness
∞	=	Freestream property

1 Introduction

In 2020, the aviation industry fixed for itself a target of carbon-neutral growth and the objective to cut 2005 CO_2 emission levels in half by 2050. As a result, the industry has seen a growth in the number of hybrid-electric propulsion systems being developed [2]. Simultaneously, advances in the power density of batteries and electric motor efficiency have enabled these new technologies to become more commercially viable. As the relationship between efficiency and power level of electric motors is relatively invariant [3], the use of distributed electric propulsion (DEP) can result in a net increase in total efficiency [4]. Many DEP systems, such as the Electrically Distributed Anti-Torque (EDAT) [5] of Bell Textron Canada Ltd., use ducted propellers in their designs. In hover, for the same thrust and power consumption, a ducted fan has a smaller diameter thus allowing for higher rotational speed at a given tip Mach number [6]. This higher angular velocity is advantageous for hybrid-electric propulsion since electric motor mass usually scales with torque [7]. Other advantages of ducted propellers include a more directional noise emission [8] and increased safety as the duct prevents blade strikes in ground operation or confined areas.

Despite the sustained progress in high performance computing, time-accurate blade-resolved (BR) simulations of open rotors remain seldom used in design and optimization processes because of their high computational cost. This problem is amplified with BR simulations of ducted geometries because of the need to resolve the boundary layers on the duct and to have a mesh fine enough to capture the strong gradients in the thin tip gaps between blades and duct. These additional considerations can represent a number of cells on the same order of magnitude as the rotor itself and render the use of BR simulations of ducted fans impractical for design and optimization purposes. With the ramping up of hybrid-electric technologies comes a growing need for numerical tools capable of simulating these systems within a duct without having to resort to BR simulations. The Actuator Line Method (ALM) presented in this paper is one of these tools that can be used to model the effect of a ducted propeller on the flow field, but with 2-3 times less cells than typical BR simulations.

The ALM was first introduced by the work of Sørensen and Shen [9] in the wind energy sector and has since then been used extensively for the study of wind farm architecture and turbine optimization. Stevens *et al.* [10] used the ALM for Large Eddy Simulations (LES) of a wind farm and showed good agreement between mean velocity profiles and experimental data. Troldborg [11] used an ALM to simulate the wake behavior and breakdown of wind turbine operating in turbulent flow from an array placed upstream. Stanly [12] used a new tip correction proposed by Martínez-Tossas and Meneveau [13] and introduced the filtered ALM which can be used on coarser-than-optimal grids while retaining accurate power predictions. Baratchi [14] used a modified ALM to simulate ducted tidal turbine performance and obtained results within the usual accuracy of the method when compared to the experimental study of Cresswell [15]. This former study used a cylindrical projection of the isotropic Gaussian kernel to respect the geometric limits of the duct. The isotropic kernel used a chord based projection factor varying from $0.6c$ to $1.2c$ with the best results obtained at $\epsilon/c = 0.6$. Baratchi concluded that smaller projection factors resulted in more precise C_T and C_P predictions at the cost of larger temporal oscillations and, in the limit, the risk of divergence as the actuating force tends to be distributed in a more singular way if the value of ϵ/c is too small. Churchfield *et al.* [16] introduced a new method of determining the effective freestream vector with the use of an integral velocity sampling (IVS), effectively removing the ambiguity of the velocity sampling location which is a troublesome area in ALM computations. In their review of velocity sampling techniques, Merabet and Laurendeau [17] identified the IVS as superior to the other velocity sampling techniques. This IVS formulation is used in the present work and will be detailed in subsequent sections. ALM simulation is not confined to the renewable energy sector; it is also used to a lesser extent in rotorcrafts and marine propulsion. Forsythe *et al.* [18] used the ALM, with the aforementioned IVS, for the coupling of a CFD solver to a flight simulator of a rotorcraft landing on a ship. Merabet and Laurendeau [19] used an ALM with IVS to simulate the hovering S-76 rotor [20, 21] and obtained similar thrust, blade loading and vortex position as in the BR simulations and experimental data, but observed a slight offset in torque and figure of merit (FoM). This discrepancy was attributed by the authors to the porous nature of the technique which makes it impossible to capture precisely all the blade-vortex interactions (BVI) leading to an overprediction of the induced velocity at the blade tip.

This work investigates the capability of an ALM using IVS to accurately compute the performance metrics of a ducted propulsion system. The method is first validated on the Caradonna & Tung open rotor [1] with varying projection factors and mesh sizes. For the ducted case, the ALM is compared to experimental wind tunnel testing and BR simulations of the same geometry inside the wind tunnel.

2 Methodology

2.1 ALM formulation

The Actuator Line Method represents the effect of a lifting surface on the flow field by adding source terms in the unsteady Reynolds-averaged Navier-Stokes equations (URANS). The lifting surfaces, in this case the blades of a propeller, are represented by rotating lines along which varying body forces are applied. Control points along the actuating line are placed at the center of a panel on which the lift and drag forces are assumed constant. Figure 1 illustrates the ALM concept where the physical blades are replaced by rotating body forces.

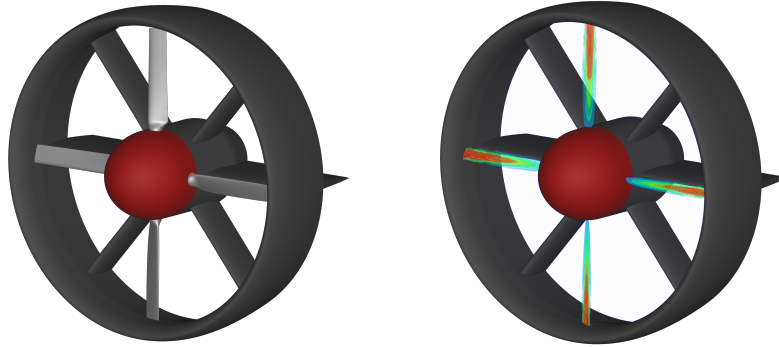


Figure 1: Geometry of the ducted fan tested in wind tunnel (left) and its ALM representation (right) via volume rendering of the actuating forces.

Flow properties are evaluated at each control point and the corresponding C_L and C_D values are interpolated from two-dimensional aerodynamic polars. The polars used in this work are generated using the open source software *Xfoil* [22]. For each Reynolds number and profile combination, the angle of attack sweep is done twice; once going from 0 to the lower bound and once going from 0 to the upper bound to ensure that the previous solution, especially near stall, does not affect the other data points. The resulting forces are spread with a kernel, here a nonisotropic Gaussian, over multiple cells to limit numerical oscillations [9, 14]. Calculations are made in a coordinate frame centered on each control point and aligned with the chord line as shown in Figure 2.

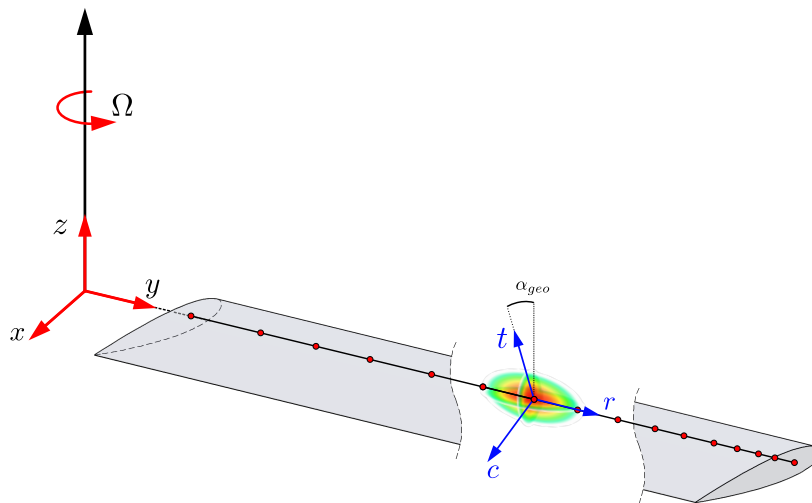


Figure 2: Actuator Line representation of a single blade showing the control points (in red) and their associated local coordinate frame (in blue).

2.1.1 Velocity sampling and force projection

Velocity sampling and force projection are the most ambiguous aspects of the ALM approach, but are crucial for the method as they can greatly impact the results [12]. Aerodynamic polars provide lift and drag coefficients as a function of the local effective *freestream* angle of attack. With the exception perhaps of simple cases such as a fixed wing in a straight flow, the location of this freestream velocity vector is ambiguous. Furthermore, the body forces accelerate (induced velocity) the flow upstream of the actuator line and create blade-local flow effects namely downwash and upwash. The flow acceleration must be taken into account by the IVS as it represents the actual velocity magnitude the blade section experiences, but local flow effects (upwash and downwash) originating from the volumetric forces should not be included in the freestream velocity vector [16]. One way of not including blade-local effects in the freestream velocity vector is to sample the velocity at the center of an isotropic Gaussian kernel. In doing so, the sampling location is at the center of the bound vorticity and the sampling is free of local effects. Martínez-Tossas [13] found that this method should be appropriate for cases with low drag, but that a correction may be needed in cases with high drag. Another solution proposed by Mittal [23] is to sample the velocity upstream of the rotor where local effects have not yet perturbed the flow. However, the sampling location is still ill-defined and the solution could suffer from time lag if the time-scale of interest is much smaller than the convective time-scale.

The IVS devised by Spalart and presented in the appendix of Forsythe [18] is an elegant solution to the problems stated above. In this IVS, the kernel $g(x, y, z)$ is used as a weight in the velocity integral as shown in Eq. 1.

$$\vec{U}_{i\infty} = \frac{\int \int \int_V g_i(x_j, y_j, z_j) \vec{U}_j dx dy dz}{\int \int \int_V g_i(x_j, y_j, z_j) dx dy dz} \quad (1)$$

where the index i stands for the control point while the index j spans all the mesh cells supporting the kernel. Any kernel $g(x, y, z)$ can be used as long as it integrates to 1. Since the kernel $g(x, y, z)$ is integrated discretely on the mesh and considered constant over each cell, the value at which $g(x, y, z)$ integrates at a given control point is never exactly one. Consequently, the sampled freestream velocity vector is normalized by the discrete value of g_i at this control point. Equation 2 provides a nonisotropic Gaussian kernel with the Gaussian widths ϵ_c , ϵ_t and ϵ_r reflecting the local airfoil geometric properties:

$$g(x_c, x_t, x_r) = \frac{1}{\epsilon_c \epsilon_t \epsilon_r \pi^{3/2}} \exp\left(-\frac{(x_c - x_{c,0})^2}{\epsilon_c^2} - \frac{(x_t - x_{t,0})^2}{\epsilon_t^2} - \frac{(x_r - x_{r,0})^2}{\epsilon_r^2}\right) \quad (2)$$

where the subscripts c , t and r refer to the coordinates in the chord-wise, thickness-wise and radial (spanwise) direction respectively while the subscript 0 denotes the center of the kernel. The Gaussian widths are related to local properties of the blade with Eq. 3:

$$\epsilon_c = a_c c_i \quad (3a)$$

$$\epsilon_t = a_t t_i \quad (3b)$$

$$\epsilon_r = a_r \delta r_i \quad (3c)$$

where c_i is the local chord, t_i the local thickness and δr_i the panel width. The parameters a_c , a_t and a_r are the projection factors used to modify the spreading of the kernel. The use of such a kernel allows the forces to be applied spatially over a volume mimicking the actual blade instead of being distributed spherically as with the usual isotropic Gaussian kernel as highlighted by the force projection isocontours shown in Figure 3. The body forces are truncated at the tip and the root to respect the geometrical boundaries of the rotor. The resulting value of g_i is used to normalize the forces and ensure that the magnitude of the applied forces is not affected by the truncation.

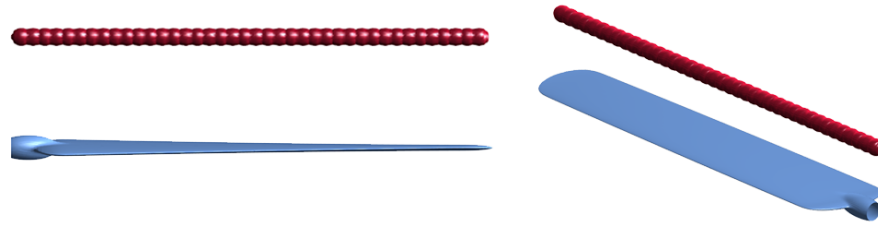


Figure 3: Force projection isocontour for the proposed nonisotropic Gaussian kernel projection (blue) and the classical isotropic Gaussian kernel (red).

In their paper introducing the IVS, Churchfield *et al.* [16] state two assumptions made in the development of their IVS formulation which are relevant to the present work. The first one is that the vorticity field is zero upstream of the rotor. While this is the case on most of the span of a ducted fan blade, it does not hold true for the outermost portion of the blade where the upstream flow has a non-zero vorticity due to the boundary layer developing on the duct inlet lip. The second assumption is that variations in the spanwise direction are small. Again, the tip of the blade is a region of the domain where this assumption might break down. It should be mentioned that the ALM is also built from a two-dimensional hypothesis regardless of the velocity sampling method used, meaning that the former assumption is already a limitation of the modelling technique.

2.1.2 Commercial solver implementation

The commercial solver *ANSYS Fluent* [24] is used to solve the URANS equations with a $k-\omega$ SST turbulence model for closure [25]. The pressure-velocity coupling is done with the SIMPLE algorithm and a second-order upwind scheme is used for spatial discretization. A second-order dual-time stepping is used for temporal integration. The ALM is added to the solution process as User Defined Functions called at various steps of each inner iteration. A relaxation factor is applied on the source terms to ensure stable convergence of the inner iterations. The solution process for the ALM involves 3 loops through all the cells of the computational domain. The first one is to integrate the kernel $g(x, y, z)$ to get the value of the discrete value of g_i , the second one is to perform the IVS at each control point and the third one is to calculate the resulting actuating forces in a cell. The first loop is done only for the first inner iteration of a time step since the discrete value of g_i is constant until the next time step. Consequently, care should be taken to limit the size of the mesh partition in which these loops are performed. In the current implementation, this can be done by separating the ALM actuating zone from the rest of the domain with interfaces such that the loops are only performed on a subset of the numerical domain.

3 Validation results

The predictive performances of the proposed ALM formulation is evaluated against the Caradonna & Tung rotor [1] on the basis of the thrust coefficient and the spanwise blade loading. Different mesh sizes and projection factors are presented to evaluate the sensitivity of the solution to these parameters. The results for the ducted case are then used to assess how the performances of the ALM change when a duct is added. More specifically, thrust and power coefficients and pressure distributions are compared with experimental data and BR simulations. Spanwise blade loading predicted by the ALM is compared with BR simulations of the wind tunnel experiment and the interaction between the duct and the ALM is commented.

3.1 Open rotor

The present ALM is first benchmarked against the experimental data of Caradonna & Tung [1]. This case is chosen for its simple geometry and the numerous cross-validations by the research community [26, 27, 28]. Table 1 summarizes the rotor geometry.

Table 1: Geometric description of the Caradonna & Tung rotor [1].

Parameter	Value
Number of blades, N_B	2
Rotor radius, R [m]	1.143
Chord, c [m]	0.1905
Root cutout [m]	0.1905
Airfoil	NACA 0012
Blade planform	Rectangular (untwisted, untapered)

The data for comparison is taken from runs at 1250 rpm which corresponds to $Ma_{tip} = 0.439$. Three collective pitch angles, 5° , 8° and 12° are simulated which corresponds to data from Tables 11, 17 and 28 respectively in the original paper. A blade-resolved simulation of the 8° case is also presented to allow a more detailed study of the spanwise blade loading.

The numerical domain is cylindrical and consists of increasingly fine refinement zones toward the ALM rotor plane as shown in Figure 4.

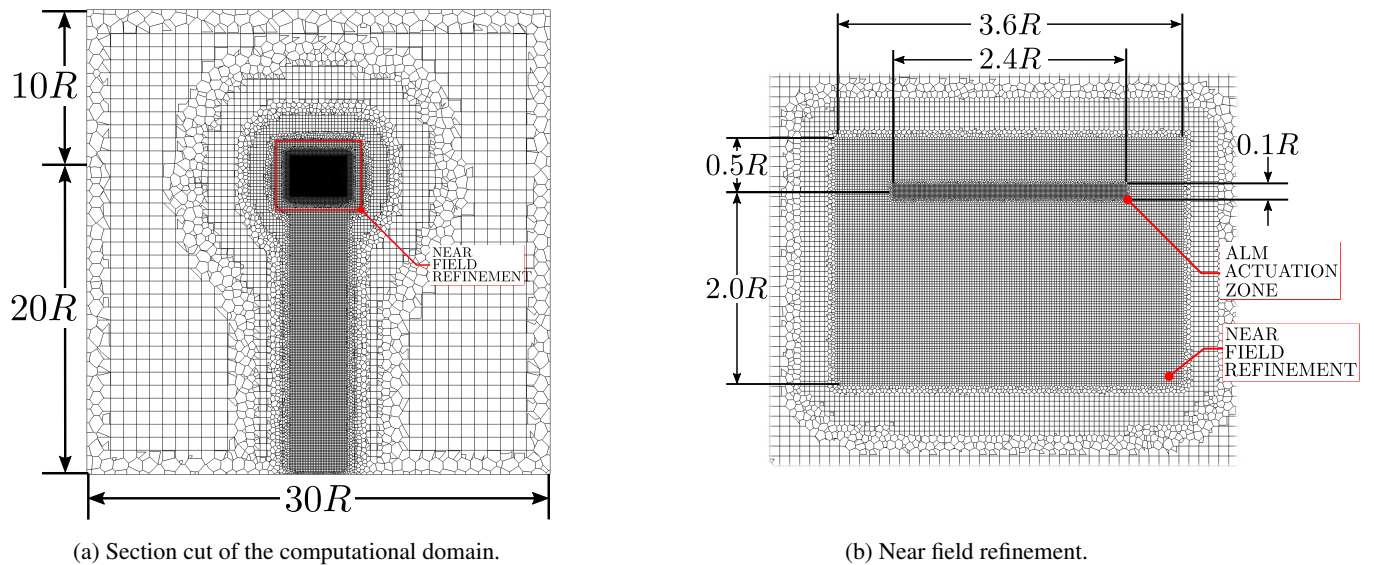


Figure 4: Computational domain for the Caradonna & Tung rotor [1].

A poly-hexcore mesh is used ensuring that all control points are within cubic (hexahedral) elements of size Δx_{ref} . One layer of polyhedral elements is inserted in each refinement zone to ensure a smooth transition in cell size and avoid 1/8 octree transitions. Table 2 summarizes the mesh sizes for the different cases. A total pressure inlet boundary condition at atmospheric conditions is applied to the top and the side of the domain and a static pressure outlet is imposed at the bottom of the cylindrical domain.

Table 2: Refinement zone size used for the Caradonna & Tung rotor [1].

Grid size	Cell count	ALM actuation zone	Near field	Wake refinement
	$\times 10^6$	$\Delta x_{ref}/c$	$\Delta x_{ref}/c$	$\Delta x_{ref}/c$
Fine (5% c)	32	0.05	0.10	0.52
Medium (8% c)	18	0.08	0.16	0.52
Coarse (12% c)	7	0.12	0.24	0.52

The blade loading predictions of the ALM are tested with 3 mesh sizes based on the chord. As reported in Table 3 and shown in Figure 6, C_T values computed by the ALM show good agreement compared to experimental data with the largest difference being for the finest mesh at the highest pitch angle. Having the maximum deviation with the finest mesh could seem like an unexpected result, but Figure 6 should be interpreted carefully. Although the velocity sampling is independent of the shape of the function $g(x,y,z)$, the flow field reacts differently depending on how the volumetric force is spread. This is supported by the work of Churchfield *et al.* [16] stating that the estimated freestream velocity is sensitive to grid resolution and body-force projection width, not because of the IVS formulation, but because of how the flow is disturbed in the vicinity of the body forces. Also supporting this is the contour of normalized vorticity on a plane coincident with a blade shown in Figure 5 for two different projection factors. As one can see, the vortex cores are bigger in the simulation with the highest value of a_c and a_t even though both simulations use the fine mesh (5% c). The dependence of the tip vortex size on the projection factors could explain why the results presented in Figure 3 were the most accurate with the coarser mesh since the tip vortex strength, and thus the resulting induced velocity, is a function of both the mesh resolution and the projection factors used.

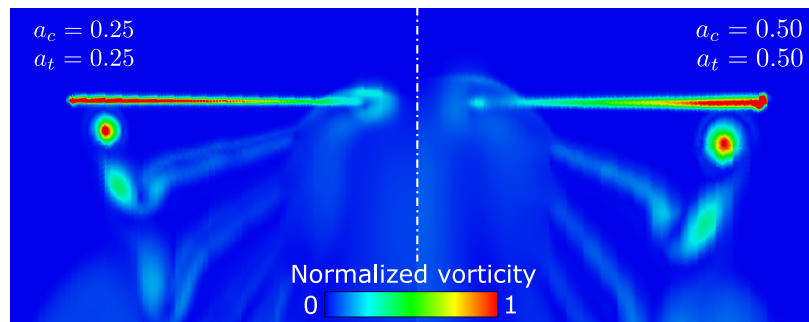


Figure 5: Contours of the normalized vorticity magnitude ($\omega c/V_{tip}$) for a pitch angle of $\Theta = 8^\circ$ coincident with a blade for $a_c = a_t = 0.25$ (left) and $a_c = a_t = 0.5$ (right).

Table 3: Thrust coefficient comparison between the Caradonna & Tung rotor and the ALM at various mesh sizes and projection factors.

	Projection factors			Collective pitch Θ		
	a_c	a_t	a_r	5°	8°	12°
BR CFD URANS					0.00453	
Caradonna & Tung [1]				0.00213	0.00459	0.00796
ALM 5% c	0.35	0.35	1	0.00224	0.00480	0.00854
ALM 8% c	0.45	0.45	1	0.00203	0.00489	0.00805
ALM 12% c	0.50	0.50	1	0.00216	0.00462	0.00806

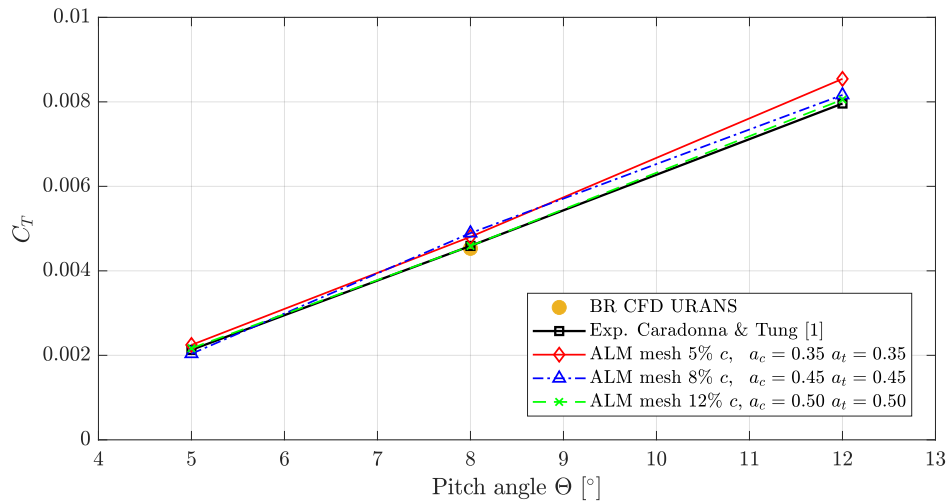


Figure 6: Comparison of the thrust coefficient computed by the ALM at three different collective pitch angles with different projection factors.

Next, the blade loading of the ALM using three different mesh sizes and projection factors is compared with BR results and the experiment of Caradonna & Tung [1]. Figure 7 shows a relatively good agreement between the BR simulation, the ALM predictions and the experimental data although one observes a slight underprediction of the loading on the first 80% span. The largest discrepancy in the results is seen in the last 10% span of the blade; the region where the tip vortex strength and the blade-vortex interaction (BVI) have the most impact. As one can see, the BVI is not well captured by the ALM, which is expected since there is no solid surface for the vortex to interact with. In the BR simulation, the low pressure at the center of the tip vortex creates a local increase in sectional thrust clearly visible in Figure 7 on the black curve near $r/R = 1$. The ALM reacts differently to the BVI by predicting a local decrease in sectional thrust. This is explained by an additional contribution of the tip vortex to the local effective freestream vector component perpendicular to the rotor plane that reduces the effective angle of attack at that location because of the porous nature of the method. Results for the 5% c and 12% c mesh show a slight increase in loading at approximately $r/R = 0.98$, but it remains much more subtle than the increase in loading due to the BVI in the BR simulation. This suggests that, for these two cases, the tip vortex has a greater intensity which entails that the weaker tip vortex for the 8% c case resulted in less downwash on the outmost portion of the blade explaining the higher tip loading. Also apparent in Figure 7 is the fact that the finer mesh of 5% c exhibits less oscillations in the spanwise loading than the two other cases.

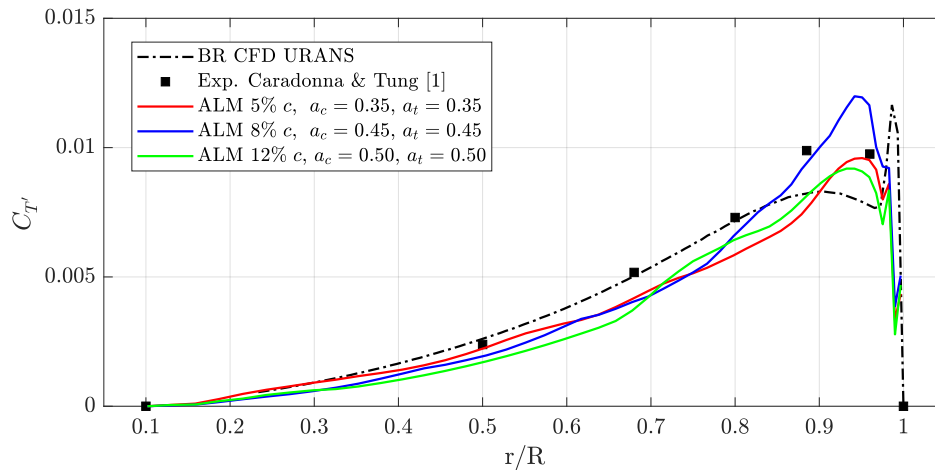


Figure 7: Sectional thrust comparison between the ALM, the experiments of Caradonna & Tung [1] and the corresponding BR URANS simulation at $\Theta = 8^\circ$.

3.2 Ducted fan

For the ducted fan case, the ALM is benchmarked against experimental data of a ducted fan tested in a wind tunnel by the industrial partner Bell Textron Canada Ltd. The experimental model was instrumented to measure rotor torque, rotor thrust and global ducted fan forces and moments. Static pressure was measured by 23 pressure taps distributed on the inner and outer surfaces of the duct at an azimuthal position of $\Psi = 0^\circ$.



Figure 8: Ducted fan tested in the wind tunnel.

Blade-resolved simulations of the duct inside the wind tunnel have also been carried out to compare the spanwise loading of the blades and to give insight regarding the vortical structures, namely the tip and root vortices, generated by the BR simulations and the ALM. In both cases, the computational domain is the same and replicates the wind tunnel geometry shown in Figure 9. A velocity inlet positioned $12R$ upstream of the ducted fan is used to control the advance ratio. The walls of the wind tunnel are modelled as slip walls to avoid the computational cost of solving the boundary layers in these regions. This should have minimal impact on the comparison with experimental data as the confinement effect of the walls is mostly potential with little impact from the boundary layers thickening.

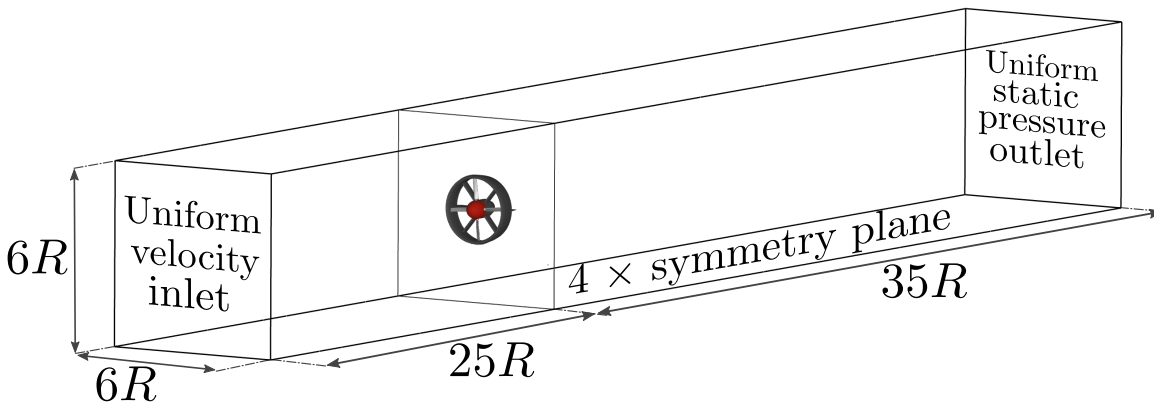


Figure 9: Computational domain for the ducted fan geometry.

Figures 10a and 10b show the thrust and power coefficient of the ALM compared to experimental data at advance ratios of 0.019, 0.057 and 0.175. The tip gap (TG) for these simulations corresponds to $3\% c_{tip}$, which is the smallest one available experimentally and thus, the most challenging to model with the ALM. The largest discrepancy in the results is on the power coefficient at the highest advance ratio where the ALM computation returns a power coefficient

of $C_p = 7.1 \times 10^{-4}$ whereas the experimental mean value is $C_p = 5.8 \times 10^{-4}$. This last result could be explained by the fact that the advance ratio of $J = 0.175$ corresponds to the operating condition where the contribution of the induced drag to the total torque is the smallest. Consequently, this is also the operating point for which the C_D obtained from the polars has the most impact on the power coefficient. Because the ducted fan operates in the transitional Re range, the position where the boundary layer transitions from laminar to turbulent greatly impacts the computed value of C_D which in turn directly affects the torque computed by the ALM. Unfortunately, the experimental nature of the dataset makes it impossible for the authors to validate this hypothesis. For all other data points, the difference between both datasets is within 10% on the averaged values.

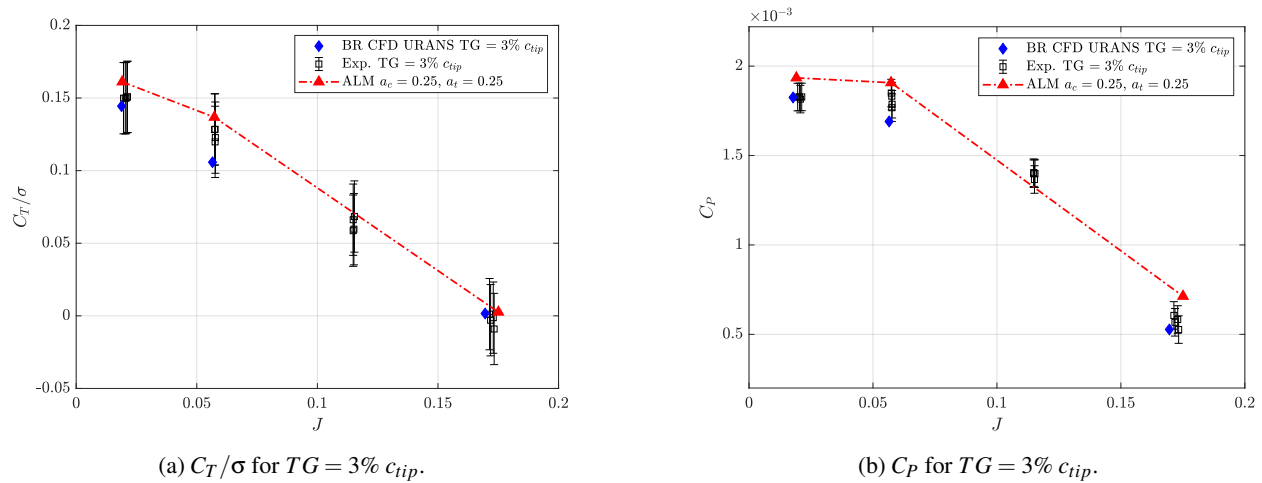


Figure 10: Performance metrics comparisons between the ALM, BR simulations and experimental data.

The most important metric for comparison is arguably the ratio of the two previously used coefficients, that is, $C_T/C_p\sigma$. Figure 11 shows a good agreement between the two datasets for the three advance ratios of interest although experimental data have a lot of scattering at $J = 0.175$. This is due to having almost no net force on the load cell compared to its uncertainty. The uncertainty presented for the experimental dataset is a lower bound uncertainty that only accounts for the uncertainty of the load cell, but does not include the uncertainty on the density, rotational speed and the ducted fan's dimensions.

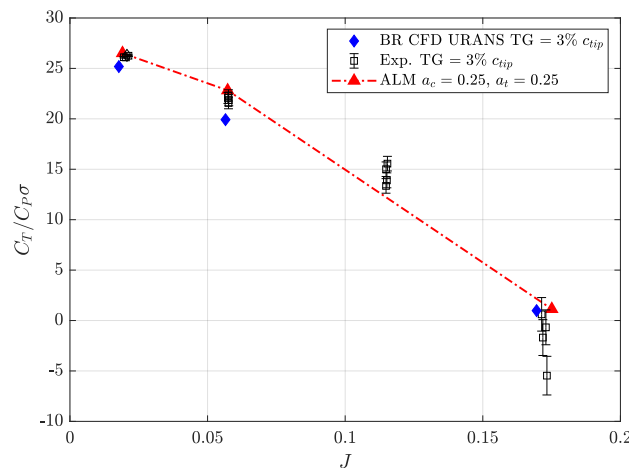


Figure 11: $C_T/C_p\sigma$ comparison of the ALM predictions versus BR simulations and experimental data for $TG = 3\% c_{tip}$.

Next, the spanwise loading of the ALM is compared to the one obtained from a BR simulation. Figure 12 shows the sectional thrust coefficient for an advance ratio of 0.057. The sectional thrust slope predicted by the ALM is similar

to the one obtained with the BR simulations until $r/R = 0.8$ where the ALM sectional thrust starts to plateau. Similar to the open rotor case, the blade loading predicted by the ALM decreases at the tip whereas it increases for the BR simulations. This is again attributed to the two completely different mechanisms by which the ALM and the BR simulations interact with the tip vortex. As previously mentioned, the porosity of the ALM allows the tip vortex to pass through the actuating line resulting in an increase in the freestream velocity vector component perpendicular to the rotor plane thus reducing the effective angle of attack. For the BR simulations, the low pressure region at the vortex core creates a local increase in thrust which is more evident in Figure 12 for the larger TG of 16% c_{tip} .

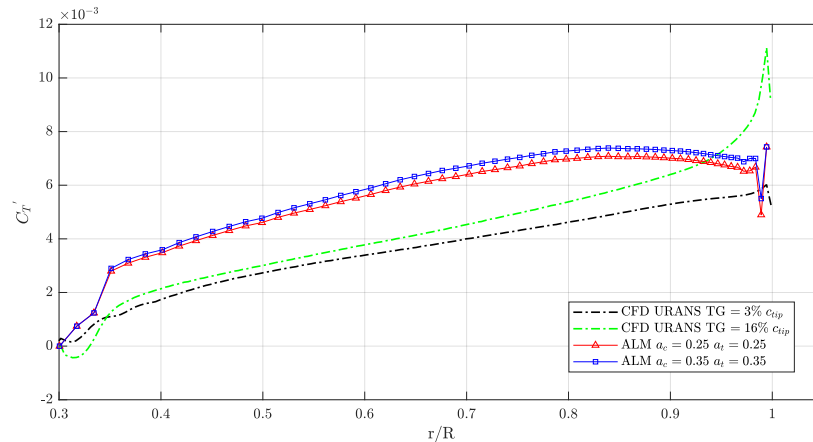


Figure 12: Sectional thrust comparison between BR simulations and the ALM at $J = 0.057$.

The constant offset between the ALM and the BR curves is to be expected since, as one can see in Figure 10a, the two simulations do not predict the same thrust, the ALM values being overestimated. Figure 13 shows a normalized vorticity contour in a plane at $\Psi = 180^\circ$ which cuts through the duct and through the blade at mid-chord for the two BR visualizations or through the actuating line for the ALM visualization. Figure 14 presents the same contours at $\Psi = 157.5^\circ$ which corresponds to a cross section of the duct midway between the blade at $\Psi = 180^\circ$ and the next stator in the anti-clockwise direction. These figures show that the ALM and the BR simulation at $TG = 16\% c_{tip}$ both predict a boundary layer separation in the diffuser of the duct which modifies its effective expansion ratio (σ_d). It should be mentioned that the present ALM does not include source terms for the turbulent quantities k and ω which might help delay boundary layer separation in the diffuser. According to the momentum theory for ducted fans in climb [29] ($J > 0$), the effective expansion ratio influences the induced velocity at the rotor plane (v_i) as shown in Eq. 4.

$$v_i = \sigma_d(w + U_c) - U_c \quad (4)$$

Equation 4 shows that the induced velocity at the rotor plane decreases with the effective expansion ratio. Consequently, this lower induced velocity increases the effective angle of attack which can explain the offset between the BR and the ALM curves in Figure 12. Figure 15 shows a normalized streamwise velocity contour for the three cases previously discussed and presented in Figure 12. Interestingly, the ALM is able to recreate the reverse flow taking place in the TG similar to the BR simulation at 3% c_{tip} , but the velocity profile after the blade differs significantly in the two cases as highlighted by the surface flow lines shown in Figure 15. Recalling the limitations of the IVS with respect to the vorticity field upstream and the two-dimensional hypothesis presented in Section 2.1.1, the difference between the ALM and the BR curves could also be explained in part by the fact that the tip region violates these limitations, but it remains unclear exactly how this would impact the results.

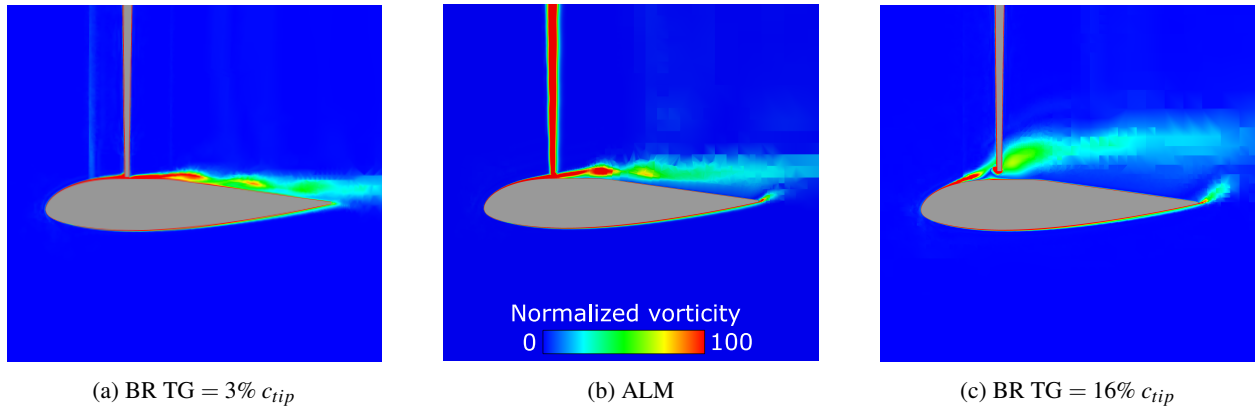


Figure 13: Contours of the normalized vorticity magnitude ($\omega c/U_\infty$) at a blade passage ($\Psi = 180^\circ$) at $J = 0.057$ for (a) the BR simulation at TG = 3% c_{tip} , (b) the ALM at a theoretical TG = 3% c_{tip} , and (c) the BR simulation at TG = 16% c_{tip} .

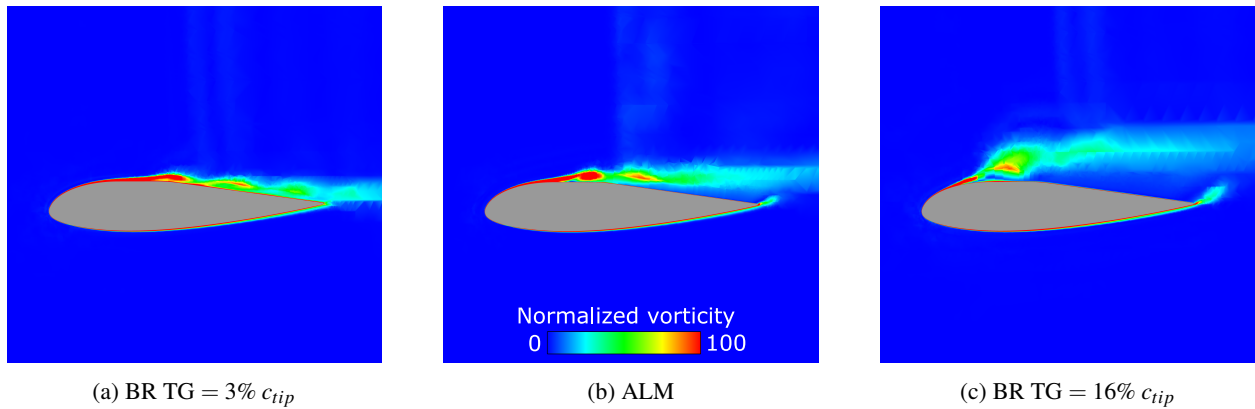


Figure 14: Contours of the normalized vorticity magnitude ($\omega c/U_\infty$) at $\Psi = 157.5^\circ$ and $J = 0.057$ for (a) the BR simulation at TG = 3% c_{tip} , (b) the ALM at a theoretical TG = 3% c_{tip} , and (c) the BR simulation at TG = 16% c_{tip} .

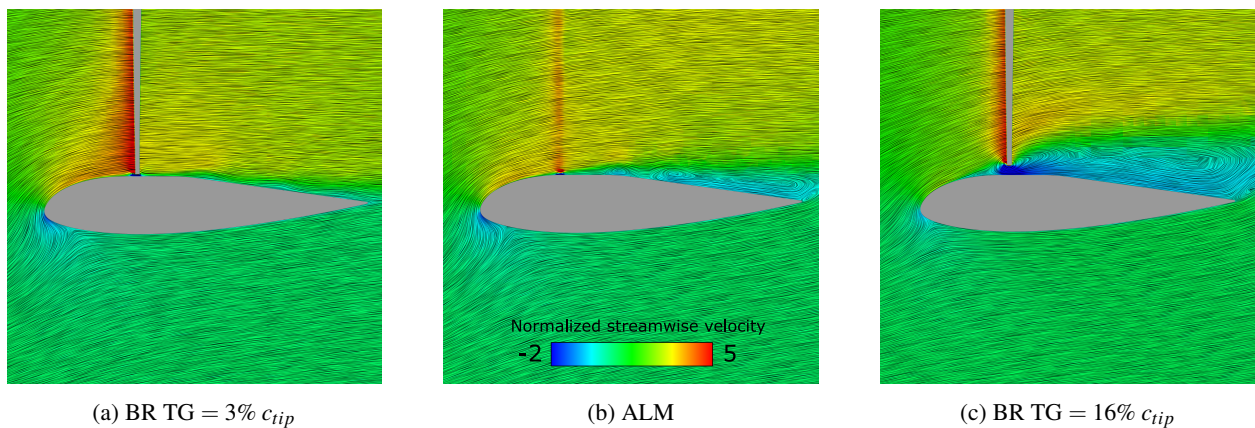


Figure 15: Contours of the normalized streamwise velocity (U/U_∞) with flow lines at a blade passage ($\Psi = 180^\circ$) at $J = 0.057$ for (a) the BR simulation at TG = 3% c_{tip} , (b) the ALM at a theoretical TG = 3% c_{tip} , and (c) the BR simulation at TG = 16% c_{tip} .

The pressure distribution about the duct in a cross-plane at $\Psi = 0^\circ$ is shown in Figure 16. The experimental data is presented for the 3 different tip gap sizes and the values shown are temporally averaged. The ALM pressure distribution is spatially averaged over the circumference of the duct by increments of 2° and 200 sample points are used to discretize the line along which the sampling is made.

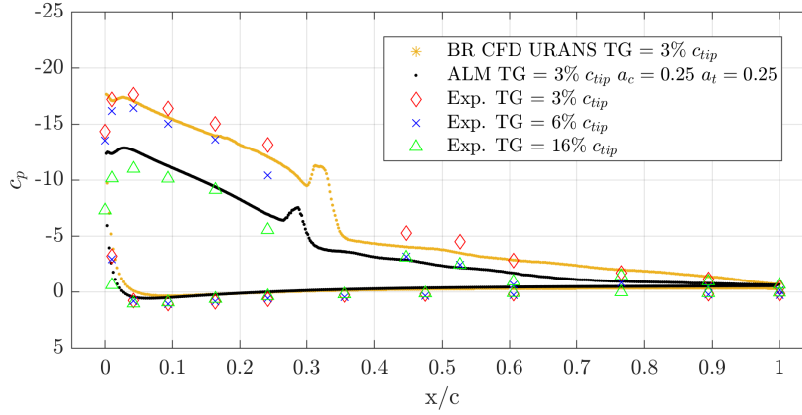


Figure 16: Averaged pressure distributions about the duct for the ALM prediction at $TG = 3\% c_{tip}$ against the BR simulation at $TG = 3\% c_{tip}$ and the experimental data for the three TG tested.

As shown in Figure 16, the pressure distribution of the ALM at $3\% c_{tip}$ is much more similar to the experimental distribution at $16\% c_{tip}$. Again, the momentum theory for ducted fans can be used to relate the differences in pressure distribution of figure 16 to the effective expansion ratio difference highlighted in Figures 13 and 14. Equation 5 shows how the effective expansion ratio influences the ratio of the rotor thrust to the total thrust of the ducted fan.

$$\frac{T_{rotor}}{T_{total}} = \frac{v_i + U_c(\sigma_d + 1)}{2\sigma_d(v_i + U_c)} \quad (5)$$

As one can see, a decrease in the effective expansion ratio results in a bigger fraction of the total thrust being produced by the rotor. As a result, the thrust produced by the duct itself is lower thus explaining the lower c_p values observed in Figure 16. For this comparison to be completely fair on the basis of the effective expansion ratio, both ducted fans should produce the same thrust which is not the case here, but Eq. 5 can still be used to give a qualitative insight of how the effective expansion ratio influences the forces on the duct and the corresponding pressure distribution. The ALM was also tested with different tip gap sizes (not shown in the present work), but showed no significant sensitivity to this parameter when varied from $1\% c_{tip}$ to $16\% c_{tip}$.

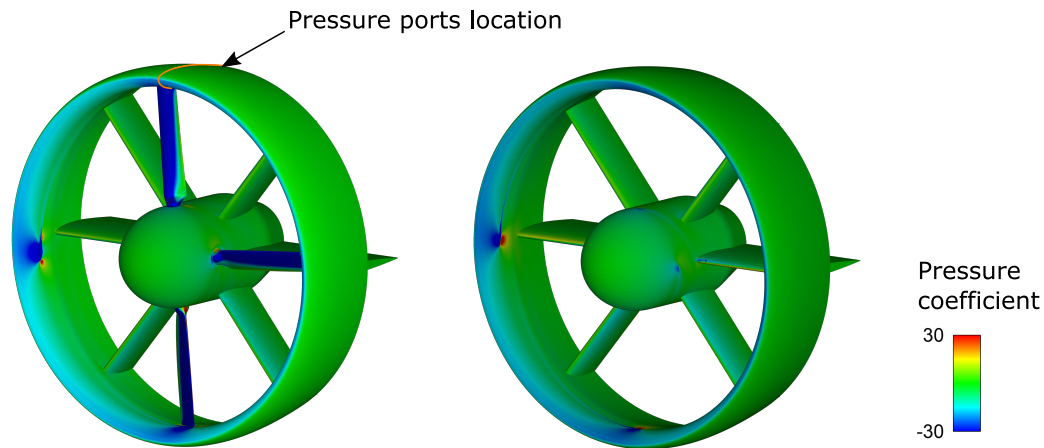


Figure 17: Comparison of the instantaneous pressure fields between the BR ducted fan (left) and the ALM (right). The blade at $\Psi = 270^\circ$ is intentionally hidden to better show the pressure coefficient of the BR simulation. A close-up view of the ducts' inner walls is provided in Figure 18 below.

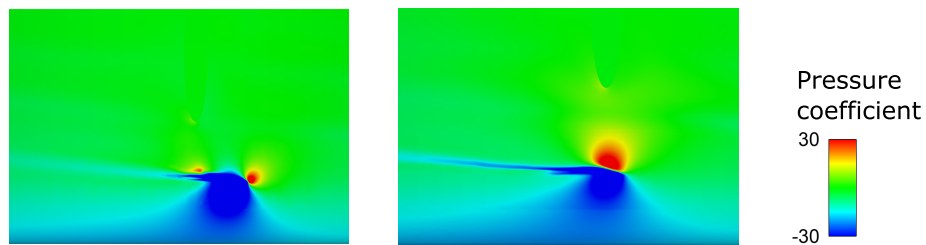


Figure 18: Close up view of the pressure coefficient on the duct's inner wall coincident with the passage of a blade for the BR simulation (left) and the ALM (right).

Figure 17 shows the pressure coefficient on the duct for the BR simulation and the ALM. In both cases, the pressure distribution is similar, but the BR simulation shows greater suction at the inlet lip which is coherent with the data presented in Figure 16. The relative position of the high and low pressure zones on the duct is also noticeably different in both cases as shown in Figure 18. For the BR simulation, the low pressure zone associated with the blade's suction side is more prominent than in the ALM simulation. The high pressure zone on the duct for the BR simulation coincides with the location of the stagnation point on the blade whereas this same pressure zone shifts towards the actuating line in the ALM simulation. This shift can also be observed in Figure 16 near $x/c = 0.3$.

Figure 19 shows a λ_2 isocontour comparison between the BR simulation and the ALM, while Figure 20 shows a close up view of this same isocontour for the blade at $\Psi = 180^\circ$. The ALM is shown to produce similar vortical structures as the BR simulation although their size and strenght differ. The root vortices in the ALM simulation are created by defining a section of the actuating line where the control point have the C_D of a smooth cylinder and zero lift. The root vortices resulting from this simplification fail to capture the complexity of flow in that region, but this is considered a limitation of the technique since ALM methods are not intended to recreate separated flow behind bluff bodies. Still, the presence of these root vortices mean they can be convected downstream and interact with the stators to create horseshoe vortices that would be significantly weaker otherwise. In the tip region, the ALM produces a slightly more diffuse tip vortex because there is no solid wall to restrict its growth. The magnitude of the vorticity in the tip vortex is also significantly weaker for the ALM, which is expected if the tip vortices are to be of similar circulation in both methods.

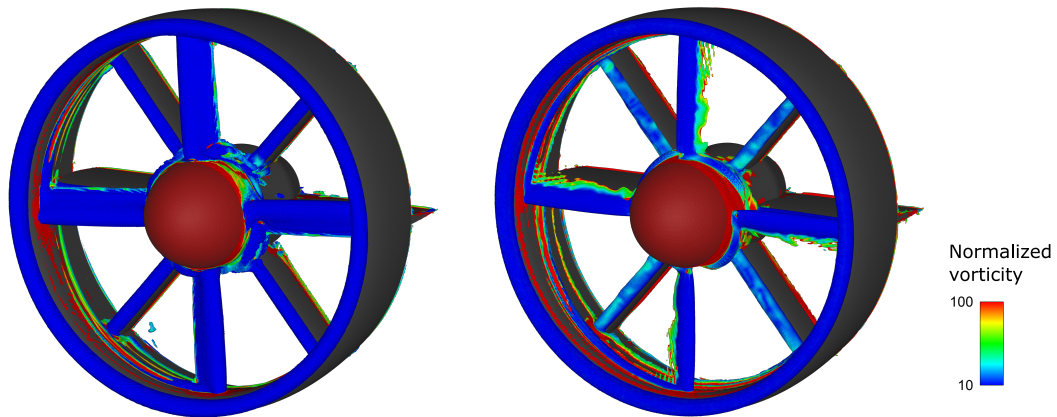


Figure 19: Comparison of the λ_2 isocontour (5×10^5) colored by normalized vorticity magnitude ($\omega c/U_\infty$) between the BR ducted fan (left) and the ALM (right).

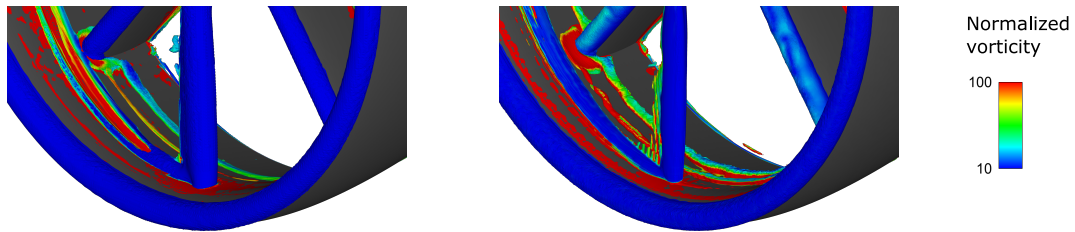


Figure 20: Close up view on the blade at $\Psi = 180^\circ$ of a λ_2 isocontour (5×10^5) colored by normalized vorticity magnitude ($\omega c/U_\infty$) between the BR ducted fan (left) and the ALM (right).

The dependence of the ALM solution to the choice of the projection factors and the mesh size is observed to be more pronounced for coarse meshes than for fine meshes. Remembering the results for the open rotor case presented in Section 3.1, the mesh sizes of $8\%c$ and $12\%c$ are relatively coarse with respect to the thickness of the airfoil. In the ducted fan ALM simulations, the mesh used is nonisotropic and much finer than for the open rotor. Although this mesh cannot be represented by a single metric as in the open rotor case, the discretization of the airfoil at the tip of the blade consists 40 cells in the chordwise direction and 20 cells in the thickness direction. Accordingly, the results are much less affected by changes in the values of a_c and a_t although some dependency remains as shown in Figure 12. Since one of the advantages of the IVS and the nonisotropic Gaussian kernel is the ability to spread forces in a way approaching the blade geometry and that the mesh is the support of the body forces, the mesh used for the ALM should be at least fine enough to represent the gross shape of the airfoil at that spanwise location.

4 Conclusion and Future Work

The present work evaluated the predictive performances of an ALM code using an integral velocity sampling method [16] applied to ducted fan geometries. Results were first validated for the open rotor of Caradonna & Tung [1] and showed accurate prediction of the thrust coefficient for the three collective pitch angles simulated. The blade loading computed by the ALM showed a similar trend to the experimental data and the BR simulation, but failed to accurately predict the loading at the tip, mostly due to the BVI and the breakdown of the two-dimensional hypothesis in that region.

When applied to ducted geometries, the ALM shows similar performance trends as the open rotor case. The computed thrust and power coefficients show good agreement with experimental data for the three advance ratios studied, although a systematic overprediction of thrust and power coefficient is observed. This discrepancy is attributed to the fact that the effective expansion ratio in the ALM simulations is less than its corresponding BR simulation resulting in a modified induced velocity at the rotor plane and a different thrust sharing between the duct and the rotor. The blade loading predicted by the ALM shows a similar trend to the BR simulations until near the tip where the BVI causes an increase in thrust for the BR simulations, but a decrease in thrust for the ALM. These different behaviours are attributed to the fact that, in the ALM, the blade-vortex interaction creates an additional velocity component perpendicular to the rotor plane that locally reduces the effective angle of attack. The results obtained in the present work suggest that the ALM is capable of a one way interaction with the duct. That is the potential effect of the duct is felt by the ALM, but the technique fails to have enough influence on the duct to have similar flow patterns on the duct's inner surface, especially in the adverse pressure gradient aft of the rotor plane. The use of an IVS in the formulation alleviated the ambiguity surrounding the sampling location in a complex rotating geometry and results have shown that the ALM applied to ducted geometries can be adequate for performance coefficient computation, but that the predictions are less accurate for more local flow effects and that the effective expansion ratio is less than what it would be in a BR simulation. Future research in the field could focus on the relationship between the projection factors and the mesh size to gain a better understanding of how they influence ALM computations. Future improvements to this model could include the addition of turbulent source terms in the code to evaluate the effect on the diffuser boundary layer and thus, on the duct's effective expansion ratio.

Acknowledgements

The authors would like to acknowledge access to the high performance computing resources of the Digital Research Alliance of Canada, Calcul Québec and Compute Ontario as well as the financial support from Mitacs in the scope of the Mitacs Acceleration Program. The authors would also like to acknowledge Bell Textron Canada Ltd. for providing experimental results, computational resources and technical expertise.

References

- [1] F. X. Caradonna & C. Tung. Experimental and analytical studies of a model helicopter rotor in hover. *NASA technical Memorandum 81232*, 1981.
- [2] Arnaud Didey Craig Hange Nathan P. Diller Johnny T. Doo, Marilena D. Pavel. Nasa electric vertical takeoff and landing (evtol) aircraft technology for public services – a white paper. Technical report, NASA, 2021.
- [3] Nicholas Borer, Michael Patterson, Jeffrey Viken, Mark Moore, Sean Clarke, Matthew Redifer, Robert Christie, Alex Stoll, Arthur Dubois, Joeben Bevirt, Andrew Gibson, Trevor Foster, and Philip Osterkamp. Design and performance of the NASA SCEPTOR distributed electric propulsion flight demonstrator. Technical report, 2016.
- [4] Mark Moore and Bill Fredericks. Misconceptions of electric propulsion aircraft and their emergent aviation markets. 2014.
- [5] Bell Textron Inc. Defining the advanced air mobility ecosystem of tomorrow.
- [6] J.G. Leishman. *Principles of Helicopter Aerodynamics*. Cambridge Aerospace Series. Cambridge University Press, 2002.
- [7] Russel Marvin, Brian Helenbrook, and Kenneth Visser. Predicting motor and generator maximum torque as a function of mass. IEEE, 2022.
- [8] H Hubbard, D Lansing, H Runyan, and N Langley. A review of rotatin blade noise technology. Technical Report problems, 1971.
- [9] Wen Zhong Shen, Jian Hui Zhang, and Jens Nørkær Sørensen. The Actuator Surface Model: A New Navier–Stokes Based Model for Rotor Computations. *Journal of Solar Energy Engineering*, 131(1), 01 2009.
- [10] Richard J.A.M. Stevens, Luis A. Martínez-Tossas, and Charles Meneveau. Comparison of wind farm large eddy simulations using actuator disk and actuator line models with wind tunnel experiments. *Renewable Energy*, 116:470–478, 2018.
- [11] Niels Troldborg, Jens N Sørensen, and Robert Mikkelsen. Actuator line simulation of wake of wind turbine operating in turbulent inflow. *Journal of Physics: Conference Series*, 75:012063, jul 2007.
- [12] Ronith Stanly, Luis Martínez-Tossas, Steven Frankel, and Yann Delorme. Large-eddy simulation of a wind turbine using a filtered actuator line model. 2022.
- [13] Luis Martínez-Tossas and Charles Meneveau. Filtered lifting line theory and application to the actuator line model. 2002.
- [14] F. Baratchi, T.L. Jeans, and Andrew G. Gerber. A modified implementation of actuator line method for simulating ducted tidal turbines. *Ocean Engineering*, 193:106586, dec 2019.
- [15] N.W. Cresswell, G.L. Ingram, and R.G. Dominy. The impact of diffuser augmentation on a tidal stream turbine. *Ocean Engineering*, 108:155–163, 2015.
- [16] Matthew Churchfield, Scott Schreck, Luis Martínez-Tossas, Charles Meneveau, and Philippe Spalart. An advanced actuator line method for wind energy applications and beyond. January 2017.
- [17] Reda Merabet and Eric Laurendeau. Parametric study on the velocity sampling techniques for the actuator line method in 2d. In *AIAA Scitech 2019 Forum*. American Institute of Aeronautics and Astronautics, jan 2019.
- [18] James R. Forsythe, Eric Lynch, Susan Polsky, and Philippe Spalart. Coupled flight simulator and CFD calculations of ship airwake using kestrel. In *53rd AIAA Aerospace Sciences Meeting*, number Company. American Institute of Aeronautics and Astronautics, jan 2015.
- [19] Reda Merabet and Eric Laurendeau. Hovering helicopter rotors modeling using the actuator line method. *Journal of Aircraft*, 59(3):774–787, may 2022.
- [20] J. Lombardi D. T. Balch. Experimental study of main rotor tip geometry and tail rotor interactions in hover - vol. 1 text and figures. Technical report, NASA, 1985.
- [21] J. Lombardi D. T. Balch. Experimental study of main rotor tip geometry and tail rotor interactions in hover - vol. 2 run log and tabulated data. Technical report, NASA, 1985.
- [22] Marc Drela. Xfoil: An analysis and design system for low reynolds number airfoils. In *Conference on Low Reynolds Number Airfoil Aerodynamics*, <https://web.mit.edu/drela/Public/web/xfoil/>, 1989.
- [23] Anshul Mittal, Kidambi Sreenivas, Lafayette K. Taylor, and Levi Hereth. Improvements to the actuator line modeling for wind turbines. In *33rd Wind Energy Symposium*. AIAA, jan 2015.
- [24] *ANSYS Fluent 2020r2 User’s Guide*, ANSYS, Canonsburg, PA, 2022.
- [25] F. R. Menter. Two-equation eddy-viscosity turbulence models for engineering applications. *AIAA Journal*, 32(8):1598–1605, aug 1994.
- [26] Abdallah Samad, Gitsuzo B. S. Tagawa, François Morency, and Christophe Volat. Predicting rotor heat transfer

- using the viscous blade element momentum theory and unsteady vortex lattice method. *Aerospace*, 7(7):90, jul 2020.
- [27] Juan D. Colmenares, Omar D. López, and Sergio Preidikman. Computational study of a transverse rotor aircraft in hover using the unsteady vortex lattice method. *Mathematical Problems in Engineering*, 2015:1–9, September 2015.
- [28] David M. Ferlisi C. and Laurendeau E. Rotor wake modelling using the vortex-lattice method. 2018.
- [29] Jason L. Pereira. *Hover and Wind-tunnel Testing of Shrouded Rotors for Micro Air Vehicle Design*. PhD thesis, University of Maryland, 2008.